

Stars with Plumbing Issues: The Formation of Collimated Outflows on Common-Envelope Simulations and Comparison to Water Fountains Observations

Sarah V. Borges* and Philip Chang

*Department of Physics and Astronomy, University of Wisconsin-Milwaukee,
3135 North Maryland Avenue, Milwaukee, WI 53211, USA*

(Dated: March 18, 2026)

Common-envelope evolution (CEE) is one of the biggest open questions in binary stellar evolution, despite being the main channel for the formation of close binaries. One of the main reasons CEE is difficult to model is the lack of direct observations that could constrain numerical simulations. One exception is luminous red novae, which are thought to represent CEEs that end in mergers. Unfortunately, there are no confirmed direct detections of ongoing events that result in the survival of a close binary, and we must rely on observations of post-CEE systems. Among these, planetary nebulae (PNe) are particularly important because their morphologies can probe how the envelope is ejected. However, post-CEE PNe do not reflect the ejected envelope in its pristine form, as winds from the central core also affect their morphology. In this context, Water Fountains (WFs), a class of objects proposed to form during CEE, provide an ideal comparison. They are identified by their collimated water masers, and most are still in the post-AGB phase. As such, WFs provide some of the best observational constraints for simulations, since they likely capture a snapshot of the envelope ejection while it is still happening. In this paper, we show that the formation of a circumbinary disk with collimated outflows surrounding the central binary arises naturally from hydrodynamical simulations of CEE, and that their morphology and kinematics are consistent with observations of WFs. We also present insights into how the properties of WFs may provide clues to understanding how CEE proceeds and help guide future simulations.

I. INTRODUCTION

Common-envelope evolution (CEE) is a brief phase in binary stellar evolution during which a giant star engulfs the companion within its envelope. The resulting drag forces extract orbital energy and angular momentum from the system, causing the orbital separation between the companion and the core to shrink. This process is responsible for forming close binaries and increases the likelihood of subsequent interactions. As a result, CEE plays a key role in the formation rates of various astrophysical systems and events, including X-ray binaries, cataclysmic variables, compact-object mergers, and Type Ia supernovae [see, e.g., 1, 2].

Despite its significance, CEE remains poorly understood. It proceeds through three main phases: the loss of orbital stability, a dynamical plunge-in, and a slower spiral-in. Each phase happens on very different timescales: the rapid plunge-in typically lasts less than a decade, whereas the slower spiral-in can last centuries to millennia. As a result, the dominant energy sources driving the interaction vary between phases. While accretion happens throughout the event, the release of orbital energy due to drag is the main driver of envelope unbinding during the plunge-in, whereas accretion may contribute significantly to mass loss and orbital decay during the spiral-in. Because of these distinct timescales and physical processes, self-consistent 3D hydrodynamical simu-

lations cannot currently model CEE from start to finish and must instead focus on one phase at a time.

The inherent lack of direct observations of ongoing CEE further complicates its modeling. Two main outcomes of CEE are possible: (i) the binary merges during the interaction, producing a luminous red nova (LRN), or (ii) the envelope is successfully ejected, leaving behind a close binary system. Among the former, V1309 Sco is the only LRN with available observations of orbital decay prior to the transient merger event [3]. For the latter, no system has been confirmed to be observed during CEE, so we must rely on post-CEE observations, such as close binaries and planetary nebulae (PNe), to constrain numerical simulations and analytical models. Close binaries primarily constrain the final separation between the core and the companion, whereas PNe can be compared with the ejected envelope.

PNe are shells of ionized gas and dust produced by isolated or binary red giants at the end of their lives [4]. Early observations with the *Hubble Space Telescope* revealed that their morphologies are more complex than the spherical structures predicted by simple hydrodynamical models [5, 6]. Approximately 80% of PNe exhibit asymmetric morphologies, and about 22% display bipolar structures [7–9]. Such bipolarity is difficult to reproduce through single-star evolution but arises naturally during CEE events. Unfortunately, the final morphology of PNe is also affected by later low-density winds from the pre-white-dwarf core [e.g., 10, 11], which complicates direct comparisons with CEE simulations.

In this context, Water Fountains (WFs) may provide a better observational class for comparison with the

* svborges@uwm.edu

ejected envelope than PNe. WFs are younger objects (most are still post-AGBs) with dynamical ages of at most ~ 200 years. They are identified by their H₂O masers, which trace fast bipolar outflows with velocities of 20–800 km s⁻¹, and 18 sources are currently confirmed [12]. WFs also host an equatorial torus containing a substantial fraction of the original envelope mass, expanding at a lower velocity. Although no close binary has been directly detected in WFs, their extreme bipolarity has long been linked to CEE. More recently, Khouri *et al.* [13] presented several arguments, beyond morphology, supporting a CEE origin despite the unconfirmed nature of the central binary. The authors noted that WFs were previously associated with intermediate-mass ($> 5 M_{\odot}$) post-AGB stars because of their high mass-loss rates ($\sim 10^{-4}$ – $10^{-3} M_{\odot} \text{ yr}^{-1}$). However, their formation rate and ¹⁸O abundances are inconsistent with this interpretation. Moreover, the oxygen-rich chemistry of WFs indicates that their envelopes were ejected before the third dredge-up could enrich the envelope in carbon. Overall, the authors argue that CEE is the only known event capable of explaining all observations above. WFs therefore may be the elusive observational constraint into envelope ejection during the spiral-in phase of CEE.

How the spiral-in phase of CEE proceeds remains an open question. Several interpretations have been proposed. In some models the interaction continues to be mediated by dynamical friction within an expanded envelope, possibly entering a self-regulated phase in which the lost orbital energy is gradually radiated away or contributes to envelope unbinding [e.g., 14, 15]. In these models the envelope is typically treated as approximately spherical, which is hard to reconcile with the bipolar morphologies observed in the post-CEE PNe and WFs. Other studies suggest that little additional orbital decay happens during this stage, either because sufficient energy was already deposited during the plunge-in phase or because of recombination energy contribution [e.g., 16–18]. However, some observations of bipolar PNe suggest that envelope ejection may occur over thousands of years rather than in a single event, which may be difficult to reconcile with models in which the envelope is ejected fast.

A final possibility is the formation of a thick circumbinary disk (CBD) in the aftermath of the plunge-in phase. The formation of a CBD during CEE has already been discussed in several studies in the literature [e.g., 19–22]. This interpretation of the spiral-in phase helps address several issues. First, it can launch collimated outflows that may last extended periods of time, naturally explains the morphology of PNe and WFs and allowing for a slower and/or episodic envelope ejection. Second, it provides a natural mechanism through which additional orbital decay may occur. From an energetic perspective, recombination energy alone is sufficient to unbind the envelope, so additional orbital decay is not strictly required. However, simulations of the plunge-in phase of CEE often predict final binary separations larger than those inferred

from observations [see discussion in 23], suggesting that interactions during the last phase of CEE may play an important role in setting the final orbital separation of post-CEE binaries.

In this paper, we show 7 simulations of CEE with a Red Giant Branch (RGB) during the plunge-in phase and onset of spiral-in and identified the formation of a CBD. With this in mind, this paper has three main objectives. (1) Provide an analytical description of the properties of the CBD that can be used as initial conditions for future simulations. (2) Compare the morphology and kinematics of the collimated outflows from CEE simulations with observations of WFs. (3) Discuss how the observational properties of WFs may give insights for future simulations and analytical models of CEE.

The structure of this paper is as follows. Section 2 presents our methods. Section 3 discusses the impact of numerics on the formation of a CBD. Section 4 defines the end of the plunge-in phase and the onset of the spiral-in phase. Section 5 describes the geometry of the central torus. Section 6 discuss the formation of collimated outflows and compares them with WF morphologies. Section 7 discusses how observations of WFs and other post-AGBs linked to CEE can give insights to future simulations. Section 8 presents our conclusions.

II. METHODS

In this work, we analyze a subset of the 3D CEE simulations presented in Borges [23]. In addition, we include one new simulation with a lower temperature floor. Table I summarizes the parameters of the simulations analyzed here. The simulations were performed with the moving-mesh hydrodynamics code MANGA [24], which is a module of the SPH code ChaNGa [25–27]. Other than CEE, MANGA has previously been used to simulate stellar mergers [24], tidal disruption events [28], and TZO formation [29].

For a more complete discussion of the methods, please refer to Borges [23]. In short, the stellar models were generated with MESA [30–35], evolved from the pre-main sequence to the red-giant branch (RGB). We considered two primary stars: a 1 M_{\odot} RGB with a radius of 78 R_{\odot} , and a 2 M_{\odot} RGB with a radius of 53 R_{\odot} . The core of the giant and the companion (initially placed at the stellar surface) were replaced by a softened point mass, and the envelope makes use of an adiabatic equation of state. The number of particles is 2 million, with 1.2 million for the star. The simulations were performed considering the HLLC solver, a floor temperature of 10^4 K, and corotation, but we also have three additional simulations to check such choices, one with the HLL solver, another with a floor temperature of 10^2 K, and a final without corotation (all for the case 2 M_{\odot} RGB, $q = 0.5$). The case with a lower floor was evolved for 3500 days, compared to the 1500 days considered in the other runs.

TABLE I. Parameters of our CEE simulations. Each set shares the same primary mass $M_{1,t}$, core mass $M_{1,c}$, and primary radius R_1 . The mass ratio is $q = M_2/M_{1,t}$ and a_f is the semi-major axis at $\epsilon = 10^{-3}$. Unless otherwise specified, the simulations use the HLLC Riemann solver, a floor temperature of 10^4 K, and assume initial corotation between the envelope and the binary.

$M_{1,t}$ (M_\odot)	$M_{1,c}$ (M_\odot)	R_1 (R_\odot)	q	a_f (R_\odot)	Run
2	0.37	53	0.25	3.5	Q025
			0.50	6.9	Q050
			0.75	11.2	Q075
			1.00	16.7	Q100
2^a	0.37	53	0.50	3.8	Q050-HLL
2^b	0.37	53	0.50	7.0	Q050-T100
2^c	0.37	53	0.50	5.7	Q050-NCR

Notes: ^a HLL Riemann solver. ^b Temperature floor of 10^2 K. ^c No corotation.

III. THE IMPACT OF NUMERICS ON THE FORMATION OF A CBD

In Fig. 1, we show the projected density for runs Q050 and Q050-HLL at $t = 40.3, 100.7, 171.1, 211.4, 302,$ and 503.4 days. Our aim is to test the impact of the Riemann solver in simulations performed with MANGA. In particular, we want to understand the reasons for the differences in the morphology between this work and Valsan *et al.* [16], who analyzed simulations of a similar system using the HLL solver and did not find evidence of collimated outflows. In the edge-on (y - z plane) view, the HLLC case develops a pronounced bipolar structure, whereas this feature is absent in the HLL case. In the HLL simulation, one side briefly shows a transient attempt to form a bipolar outflow, but this structure is later disrupted and does not persist.

In Fig. 2, we present histograms of mass as a function of $\cos\theta = z/r$ within a radius of $700 R_\odot$ at two different times. The HLLC simulation maintains an approximately axisymmetric morphology throughout the evolution, whereas the HLL becomes asymmetric. The HLLC solver is known to capture contact discontinuities more accurately than HLL. The improved treatment of contact discontinuities in HLLC therefore allows the collimated outflows to form and remain coherent for longer periods of time. In contrast, the more diffusive HLL solver tends to smear out such discontinuities, which can suppress the formation or long-term survival of the outflows.

Moreover, in Fig. 2 we show that the mass in the close vicinity of the binary decreases with time, although this decrease is more pronounced in the HLL case. This may be connected to the amount of energy transferred to the system. In Fig. 3, we show the evolution of the orbital separation and the unbound fraction for both solvers. The unbound fraction is computed using the sum of mechanical (E_{mech}) and internal (E_{int}) energies for each particle i ,

$$E_{\text{tot}} = E_{\text{mech}} + E_{\text{int}}. \quad (1)$$

Particles with $E_{\text{tot},i} < 0$ are considered bound to the system, whereas those with $E_{\text{tot},i} > 0$ are considered unbound. For more details, see Borges [23] and Prust and Chang [17].

As initially discussed in Borges [23], the two solvers produce significantly different orbital evolution. In the HLL run, the final separation is smaller ($3.8 R_\odot$ versus $6.9 R_\odot$), which allows the binary to deposit more orbital energy into the envelope and unbind it faster. By the end of the simulation, nearly 100% of the envelope is unbound in the HLL case, whereas the HLLC run reaches only slightly above 60%. This difference likely also has a direct impact on the formation of collimated outflows. In the HLL case, the envelope is removed too fast for long-lived collimated structures to develop. In contrast, the HLLC run still have substantial amount of mass in the equatorial region and this remaining material can then reorganize into a CBD and provide a reservoir that feeds the polar outflows.

These results illustrate that the outcome of CEE simulations can be highly sensitive to numerics and to the final separation reached after the plunge-in phase. This sensitivity may help explain why some simulations in the literature report the formation of long-lived CBD structures and collimated outflows, whereas others do not. In this context, observational constraints become particularly valuable and suggest that configurations similar to our HLLC runs are more consistent with observed systems and thus, trustworthy.

IV. THE ONSET OF THE SPIRAL-IN PHASE

The transition between the plunge and spiral-in is often identified using the condition:

$$|\dot{a}P/a| < \epsilon, \quad (2)$$

where a is the semi-major axis, P is the orbital period between core and the companion, and ϵ is a threshold value, typically 0.1 or 0.01. This criterion was introduced as a practical way to distinguish the rapid orbital decay of the plunge phase from the subsequent slower spiral-in. However, the physical meaning of this boundary remains debated [see, e.g., 1]. If the spiral-in phase is interpreted as a self-regulated continuation of drag-driven evolution, the distinction may be largely operational, reflecting a gradual decrease in drag due to the envelope puffing-up rather than a sharp boundary in the underlying physical regime. In contrast, if a CBD forms, the transition between phases is not defined only by a reduction in orbital decay, but by a qualitative change in the morphology of the system. From this perspective, morphological indicators can provide a more physically motivated definition

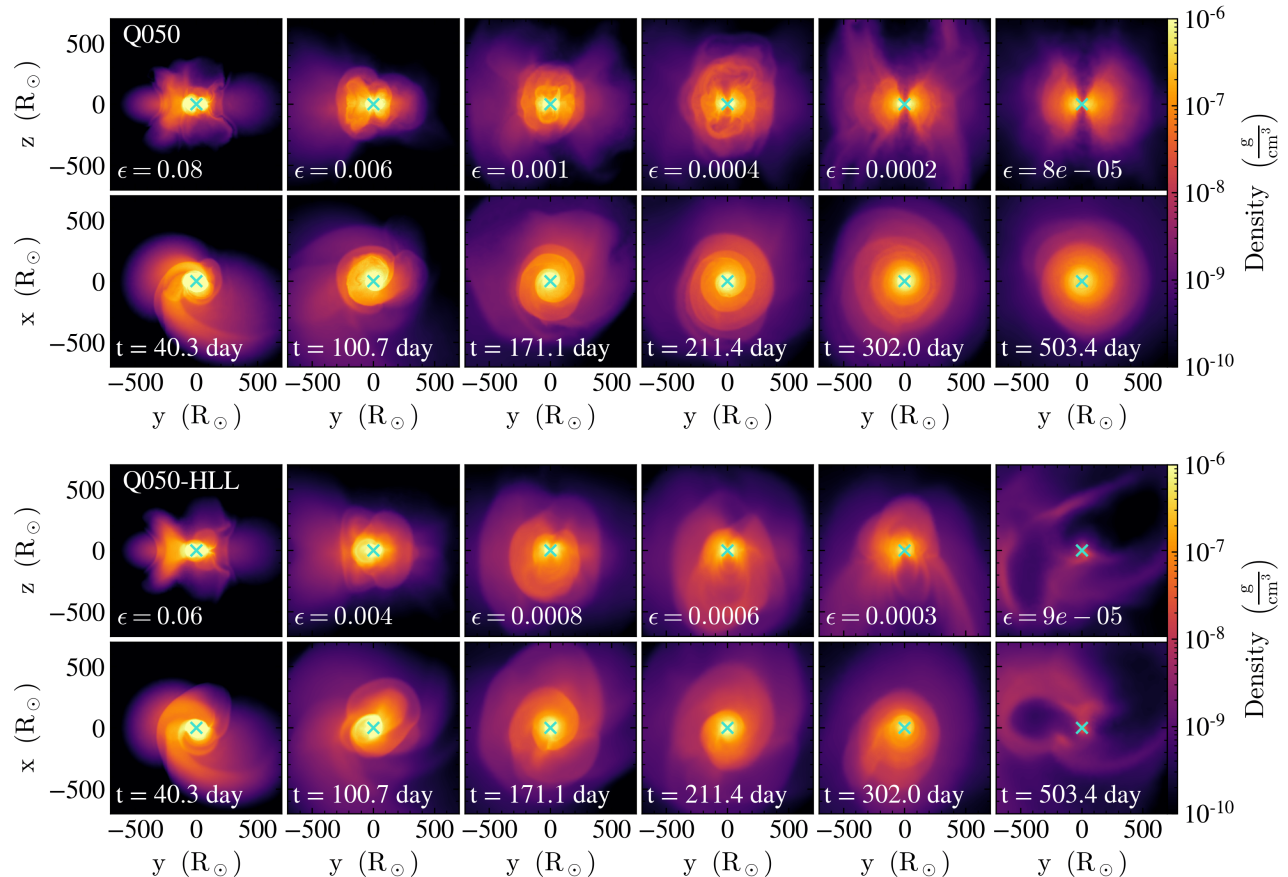


FIG. 1. Density distribution for a $2 M_{\odot}$ RGB star in a binary system with mass ratio $q = 0.5$. Top: Q050 run, HLLC Riemann solver; bottom: Q050-HLL run, HLL Riemann solver. Each panel shows both y - x and y - z views at times $t = 40.3, 100.7, 171.1, 211.4, 302, \text{ and } 503.4$ days. Each panel have the ϵ at that given time. The cyan 'x' marks the center of mass of the core+companion duo.

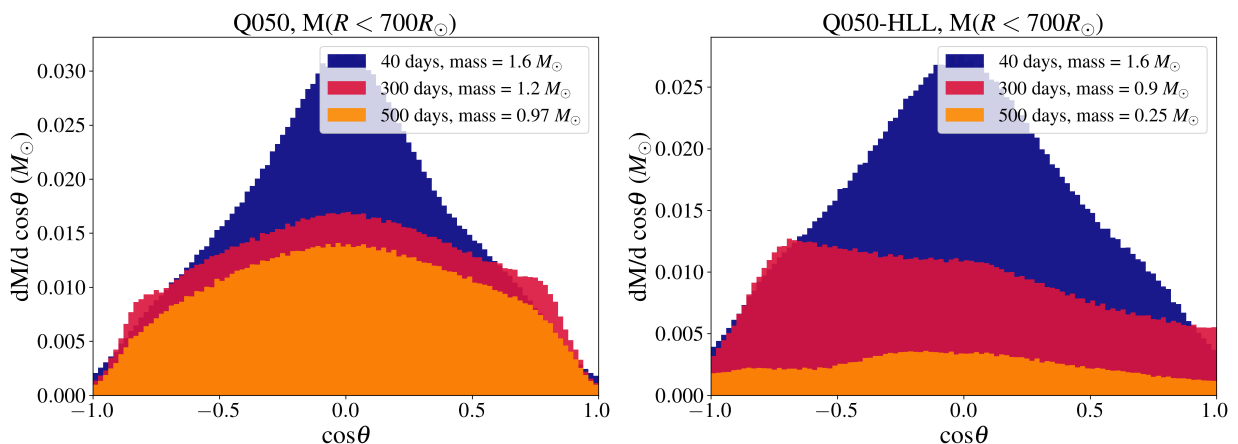


FIG. 2. Envelope mass distribution per $\cos(\theta)$ for a radius of $700 R_{\odot}$ around the center (which is the size of the box of Fig. 1) of mass of core+companion due for the $2 M_{\odot}$ RGB star, $q = 0.5$, at 40 (blue), 300 (red) and 800 (orange) days. Left panel: Q050 run, HLLC solver. Right panel: Q050-HLL run, HLL solver.

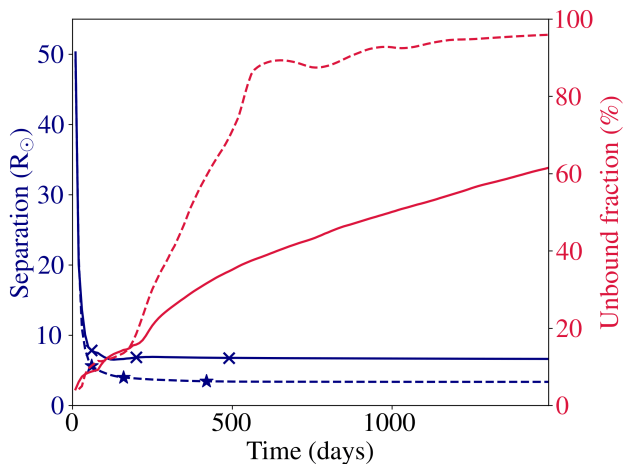


FIG. 3. Evolution of the unbound fraction (red) and orbital separation (blue) for a $2 M_{\odot}$ RGB star with $q = 0.5$. Solid and dashed lines represent simulations using the HLLC (Q050 run) and HLL (Q050-HLL run) Riemann solvers, respectively. The markers 'x' and '*' indicate the times at which $\epsilon = 0.01$, 0.001, and 0.0001 are reached for the HLLC and HLL runs, respectively.

of the change. In our HLLC runs, we define the beginning of spiral-in as the moment in which a CBD is formed and the polar outflows emerge.

For run Q050, for instance, this happens at approximately 200 days, respectively, corresponding to $\epsilon \sim 10^{-3}$ (see Fig. 1). This suggests that the commonly adopted threshold ($\epsilon = 0.01$) identifies a boundary that precedes the transition associated with disk formation. Although we still find that defining the separation between phases through equation 2 is advantageous as a standardized way to compare simulations, we advocate adopting a stricter value of $\epsilon = 10^{-3}$ (or even 10^{-4} to allow the disk and outflows time to adjust).

A stricter threshold is also consistent with the fact that the plunge phase proceeds much more rapidly than the spiral-in phase. It is therefore better for the threshold to extend slightly into the spiral-in phase rather than into the plunge. For example, if the physical transition happens at 200 days, selecting 250 days as the beginning of the spiral-in phase is better than selecting 150 days, since the state of the system at 250 days is more similar to that at 200 days than the state at 150 days.

V. FORMATION OF A THICK DISK

This section follows a similar approach to Ivanova and Nandez [15] and Valsan *et al.* [16] by providing an analytical description of the envelope immediately after the plunge phase of CEE. However, unlike those works, our simulations indicate the formation of a CBD rather than a spherically symmetric expanding envelope. It also holds similarities to Vetter *et al.* [21], that described a CBD from a CEE simulation, with the difference that

we have a low-mass RGB instead of a supergiant, don't use MHD in the simulations, and analyze different mass ratios.

Ideally, a fully self-consistent simulation would model both the plunge phase and the subsequent spiral-in phase. Nevertheless, as discussed earlier, the final phase of CEE may require the inclusion of additional physical processes (such as accretion onto the central binary), which may make it advantageous to simulate these phases separately and thus, we believe that our analytical description can be useful for future works. We analyzed the runs Q025, Q050, Q075, Q100, and Q050-NCR at $t = 500$ days, and for Q050-T100 at $t = 500$ days and $t = 1500$ days. We've chose 500 days to allow for all runs to reach the spiral-in phase. We do not analyze the Q050-HLL run because, as shown in Sec. III, it does not form a CBD. The analysis gives extra emphasis to the run Q050-T100 and displays the others for comparison.

The impact of a thin CBD on the orbital separation of a central binary has been widely studied and can, in principle, either widen or shrink the orbit [36, 37]. Tiede *et al.* [38] showed that the outcome can depend on the disk thickness, but their study explored aspect ratios only in the range $H/r = 0.01-0.1$. In contrast, the CBD produced during CEE immediately after the plunge phase has $H/r \sim 0.4-1$ [see Fig. 5; also 21], which remains, to our knowledge, a largely unexplored region of parameter space. We therefore argue that studies focusing on the evolution of thick CBDs similar to those formed in our simulations can provide valuable insight into the final phase of CEE, even if they do not reproduce the full process self-consistently.

To conclude, we emphasize that the thick CBD formed shortly after the plunge differs from the post-CEE thin CBDs analyzed in previous works [e.g., 39-41]. As noted by Wei *et al.* [40], a thick disk produced during CEE is expected to evolve into a thin disk on timescales of a few centuries. Since CEE is a transient phase, the thick CBD should likewise be regarded as a transient structure that may exhibit dynamical instabilities. For this reason, it is more natural to interpret the thick CBD as the final stage of CEE evolution, whereas the thin disks discussed in previous studies are better interpreted as post-CEE structures. In this framework, we should see the end of CEE happens when the thick disk disappears, either because it transitions into a thin disk or because the disk material is exhausted.

A. Radial Scaling of Density

At a given location, the density of the disk can be approximated as

$$\rho(R, z) = \rho_0(R) \exp\left(-\frac{z^2}{2H(R)^2}\right), \quad (3)$$

where $\rho_0(R)$ is the mid-plane density and $H(R)$ is the

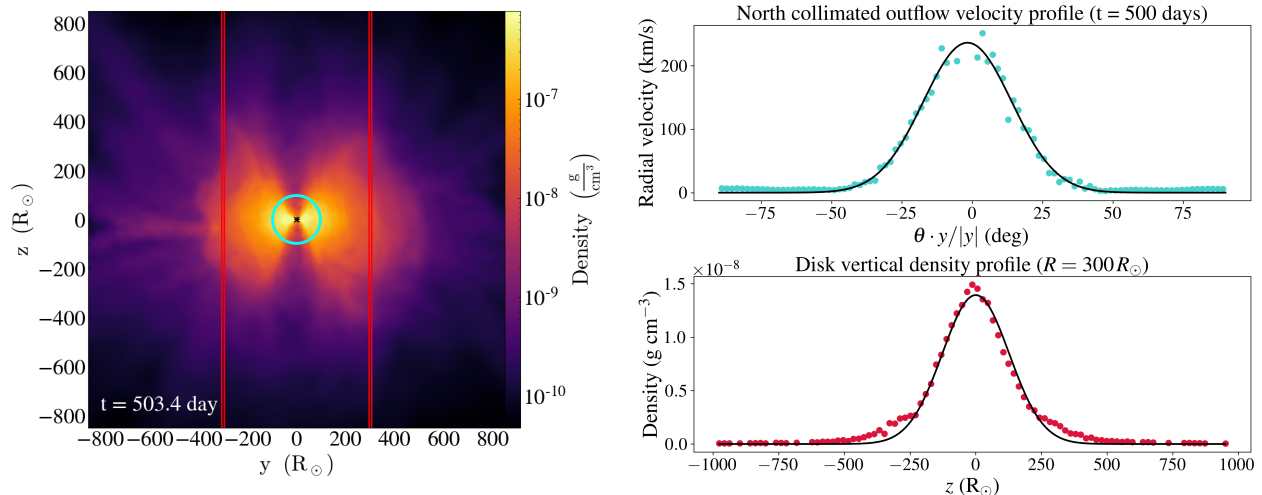


FIG. 4. *Left*: Density distribution for a $2 M_{\odot}$ RGB star in a binary system with mass ratio $q = 0.5$ in the y - z plane at $t = 402.7$ days. The cyan circle marks the spherical slice with radius $100 R_{\odot}$ around the center in which the radial-velocity Gaussian is calculated over θ (see Sec. VI). The red lines mark the slice of the cylinder with radius $300 R_{\odot}$ in which the density Gaussian is calculated over z (see Sec. V A). *Right*: Gaussian fits for the velocity distribution over θ (top) and the density distribution over z (bottom).

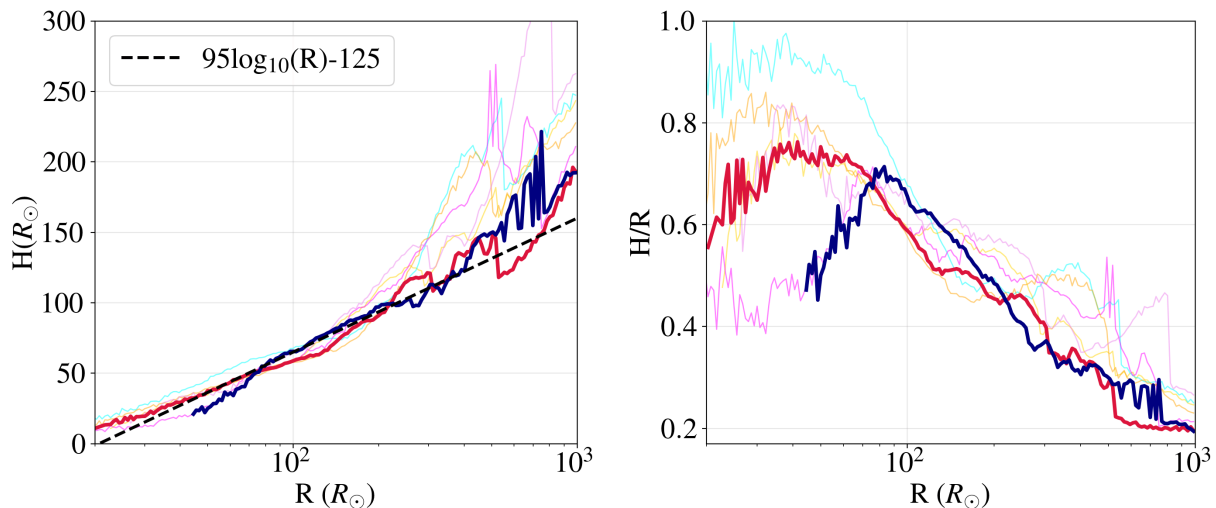


FIG. 5. *Left*: Disk height H as a function of radius for the runs Q025, Q050, Q075, Q100, and Q050-NCR at $t = 500$ days (faint lines), together with Q050-T100 at $t = 500$ and 1500 days (red and blue bright lines, respectively). The black dashed line shows the best linear fit to the Q050-T100 profile at $t = 500$ days. *Right*: Disk thickness H/R as a function of radius for the same runs.

vertical scale height of the disk at radius R . Both quantities are estimated by fitting a Gaussian profile to the vertical density distribution within thin radial bins. The radial bins are constructed in logarithmic space, using 200 bins between 10 and $1000 R_{\odot}$. For each bin we compute the vertical density profile and determine $\rho_0(R)$ and $H(R)$ from the best-fitting Gaussian. The fact that the vertical density structure is well described by a Gaussian profile is consistent with a disk-like configuration. The resulting values of $H(R)$ and the corresponding aspect ratio H/R are shown in Fig. 5.a and b, respectively. For

the Q050-T100 run, $H(R)$ is well fitted as:

$$H(R) = (95 \times \log_{10}(R) - 125) R_{\odot} \quad (4)$$

We note that beyond a certain radius the envelope is no longer well represented by a Gaussian profile. This transition can be seen in Fig. 5, where the curves for $H(R)$ and H/R show a sudden drop. For instance, for the run Q050-T100 at 500 days this happens at $\sim 500 R_{\odot}$, while at 1500 days it happens at $\sim 800 R_{\odot}$. We interpret

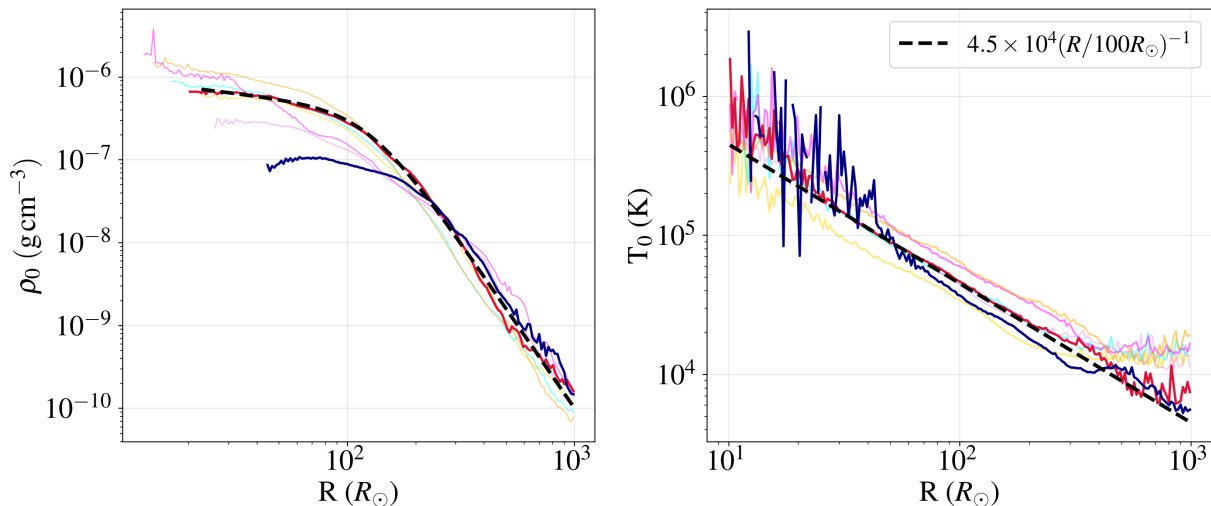


FIG. 6. *Left*: Central density ρ_0 as a function of radius for the runs Q025, Q050, Q075, Q100, and Q050-NCR at $t = 500$ days (faint lines), together with Q050-T100 at $t = 500$ and 1500 days (red and blue bright lines, respectively). The fit from Eq. 3 is shown in a black dashed line. The dashed black line show the corresponding analytical fit. *Right*: Central temperature T_0 as a function of radius for the same runs. In all cases, the temperature approximately follows $T_0 \propto R^{-1}$.

this as the outer radius of the disk. Beyond this point, there is still envelope but it does not behave as a disk.

In Fig. 7.a we also show the radial evolution of $\rho_0(R)$. Unlike the height profile, which follows a straight line in log-space, the density profile does not admit a simple functional form. For the Q050-T100 run, a reasonable approximation is

$$\rho_0(R) = 10^{-2} \left(\frac{R}{10 R_\odot} \right)^{-4} \times \left[1 + \left(\frac{125}{R} \right)^{3.5} \right]^{-1.05} \text{ g cm}^{-3}. \quad (5)$$

For the other mass ratios we did not attempt to derive an analogous analytical fit. Instead, we provide the density profiles shown in Fig. 6.a in the data files accompanying the paper. The functional form above reflects two main regimes for the central density. At large radii the term $(R/10 R_\odot)^{-4}$ dominates, while at smaller radii the second factor becomes important. This behavior reflects the presence of two distinct components in the ejecta: a thick disk and an expanding component.

B. Radial Scale of Temperature

Figure 7 shows the temperature distribution in the x - y and y - z planes for the Q050-T100 case, in which we can see the region of the collimated outflows as well as the disk increasing its outer radius over time. We also examined the vertical temperature structure. Unlike the density, which follows a Gaussian profile, the temperature exhibits a more complex behavior in the z -direction,

with a double peak near the mid-plane. To determine the radial scaling of the mid-plane temperature (T_0), we therefore consider a region with $|z| < 0.01R$ and compute the average temperature within this region.

In fig. 6.b, we show the radial profiles indicate that the mid-plane temperature follows a power-law behavior, $T(R) = A(R/100R_\odot)^{-1}$. For the runs with a 10^4 K floor temperature, we can see T_0 reaching a plateau at around $500 R_\odot$. Before this point, we did not see a difference between the runs with different floor temperatures. While the slope of the profile is consistent across the simulations, the normalization varies with the binary mass ratio. In our models the coefficient A is approximately 4.5 for the $q = 0.5$ simulations (Q050 and Q050-T100).

C. Azimuthal and Radial Velocity Components

In Fig. 9.a we show that the central CBD initially exhibits mostly sub-Keplerian rotation, as expected given its relatively large mass and high aspect ratio. In such a thick and massive disk, gas pressure contributes to reducing the orbital velocity below the purely Keplerian value. We also note that the mass ratio influences how much the disk deviates from a purely Keplerian profile. For $q = 1$, v_ϕ/v_{kep} is around 0.8–1 for most of the disk, while for $q = 0.25$ this ratio ranges from 0.2–0.5. Comparing the runs with and without corotation ($q = 0.5$), we find that corotation does have an effect, although it is smaller than that of the mass ratio.

Moreover, Fig. 8 shows the direction of the gas streamlines. At 500 days, for $R \lesssim 500 R_\odot$ the flow is predominantly azimuthal in the x - y plane, although it does show some radial component at larger radii. In the y - z plane

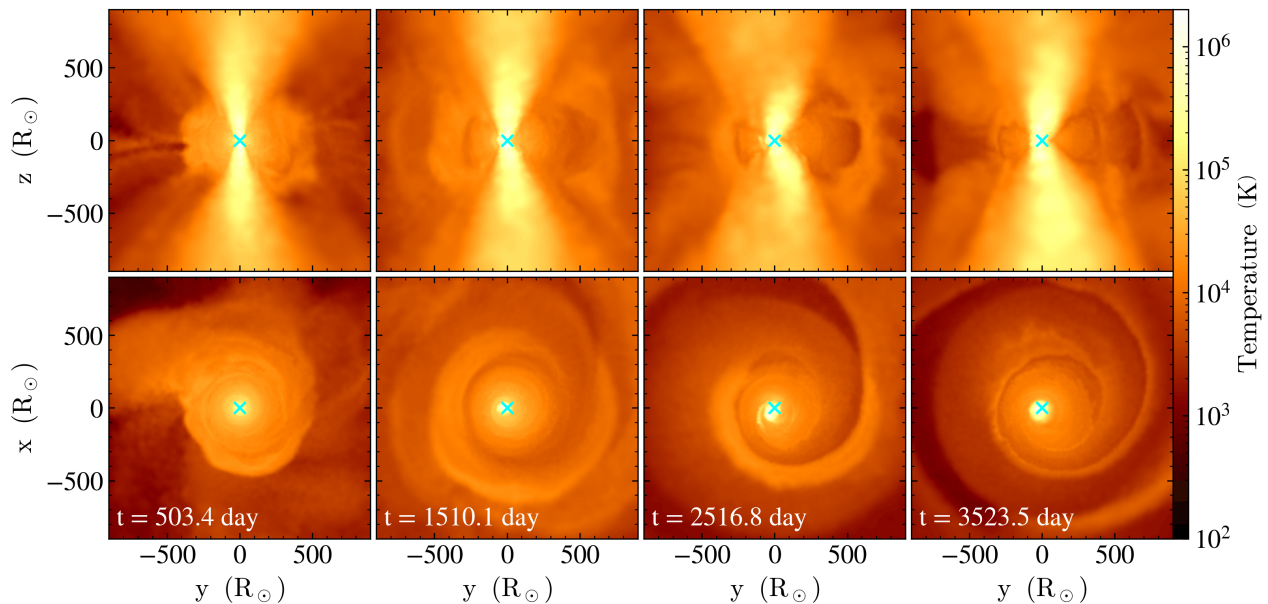


FIG. 7. Temperature distribution for a $2 M_{\odot}$ RGB star in a binary system with mass ratio $q = 0.5$, for a floor temperature of 100 K (Q050-T100 run). Each panel shows both y - x and y - z planes at times $t = 503.4$, 1510.1, 2516.8, and 3523.5 days. The cyan 'x' marks the center of mass of the core+companion binary.

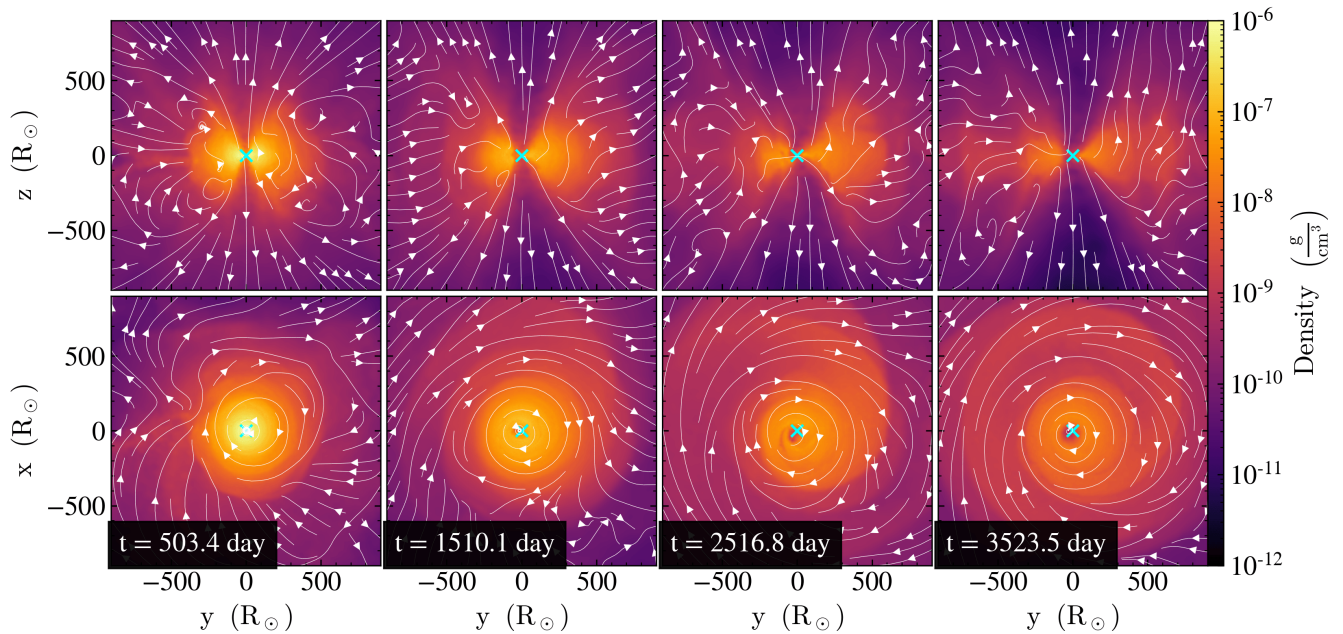


FIG. 8. Density distribution for the same run (Q050-T100), planes, and times as Fig. 7. White streamlines indicate the projected gas velocity field (v_x - v_y in the y - x plane and v_y - v_z in the y - z plane). The cyan 'x' marks the center of mass of the core+companion binary.

we can also identify the region of the collimated outflows, where the streams are mostly radial. It is also possible to see the disk spreading and increasing its outer radius.

In Fig. 10.a we plot the radial velocity component v_r as a function of radius. As shown, v_r remains close to zero within the inner $\sim 500 R_{\odot}$ and then increases with ra-

dius as the flow becomes progressively more radial. This high-speed outer part of the ejecta is composed of envelope material that was ejected ballistically during the radial plunge. In Fig. 10.b we further examine how the kinetic energy is distributed among velocity components as a function of radius. At small radii the kinetic en-

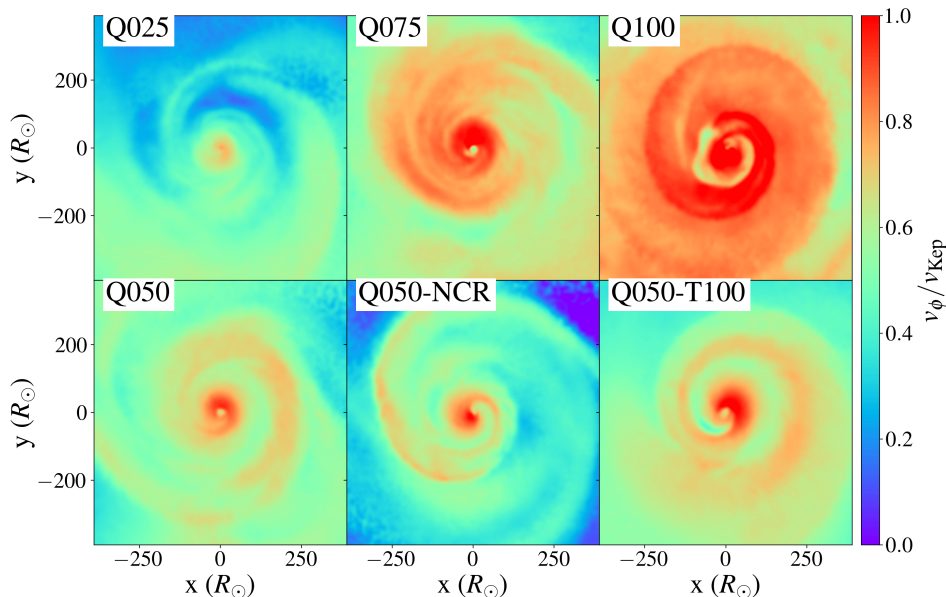


FIG. 9. Ratio v_ϕ/v_{Kep} in the x - y plane at $t = 500$ days for the runs Q025, Q075, Q100, and Q050 (top panels), and Q050-NCR and Q050-T100 (bottom panels).

ergy is dominated by the azimuthal component, consistent with the presence of the disk. For the Q050-T100 run (at 500 days), around $\sim 600 R_\odot$ the radial component begins to dominate, and for $R \gtrsim 2000 R_\odot$ the kinetic energy is 100% radial. This behavior is consistent with the picture described above: the envelope behaves as a CBD out to a radius of $\sim 500 R_\odot$ (at 500 days), while the outer envelope consists of material that was initially ejected ballistically. At 1500 days, this transition happens around $1000 R_\odot$.

VI. FORMATION OF COLLIMATED OUTFLOWS AND COMPARISON TO WF'S

Observations of WFs also indicate the presence of massive equatorial structures, such as CBDs. For example, IRAS 15103–5754 and IRAS 16342–3814 are estimated to host equatorial tori with masses of 0.4 – $1.0 M_\odot$ and $\sim 1 M_\odot$, respectively [42, 43]. For the CBD, however, the only quantity that can be meaningfully compared with our simulations is the total mass. These estimates are uncertain and model dependent, but they nevertheless indicate that in both cases a massive structure is present in the orbital plane.

The collimated outflows provide more observable quantities that can be compared with the simulations, such as the outflow speed, opening angle and bipolar morphology. Nevertheless, as in the case of the CBD mass, these comparisons can only be made at the order-of-magnitude level, given that the masses of the central stars are not known, and these quantities are expected to evolve during the ~ 200 yr lifetime of WFs. Thus, in this section, we describe the properties of the collimated outflows and

compare them with observations of WFs.

A. Opening angle of the outflow

In Fig. 12.a we show the evolution of the opening angle of the outflow as a function of time for all simulations using the HLLC solver. To estimate the opening angle, we select a spherical shell with a radius between 95 and $100 R_\odot$, located near the base of the outflows. The velocity field within this shell is binned into 100 angular segments, and the resulting distribution is fitted with a Gaussian profile. The opening angle is then defined as 2σ of the Gaussian distribution (see Fig. 4 for an illustration of the Gaussian fit and the circle at $100 R_\odot$).

The opening angle increases slightly over time, evolving from $\sim 30^\circ$ to approximately 40 – 50° . Compared to previous work, MHD simulations typically find narrower outflows. For example, Vetter *et al.* [44] reported opening angles of 16 – 24° in their MHD simulations of a CEE event involving a red supergiant. However, a direct comparison is difficult because different methods are used to estimate the opening angle (see their Sec. 3.3). Interestingly, the angles obtained in our simulations are closer to those inferred for WFs. For instance, IRAS 15103–5754 and IRAS 18043–2116 have observed opening angles of 56° and 60° , respectively [42, 45]. Given the different techniques used in simulations and observations, an exact agreement is not expected. In our case the opening angle is derived from hydrodynamical quantities, whereas observational estimates depend on radiative diagnostics. Nonetheless, both approaches indicate relatively wide outflows.

It is also worth noting that our simulations do not

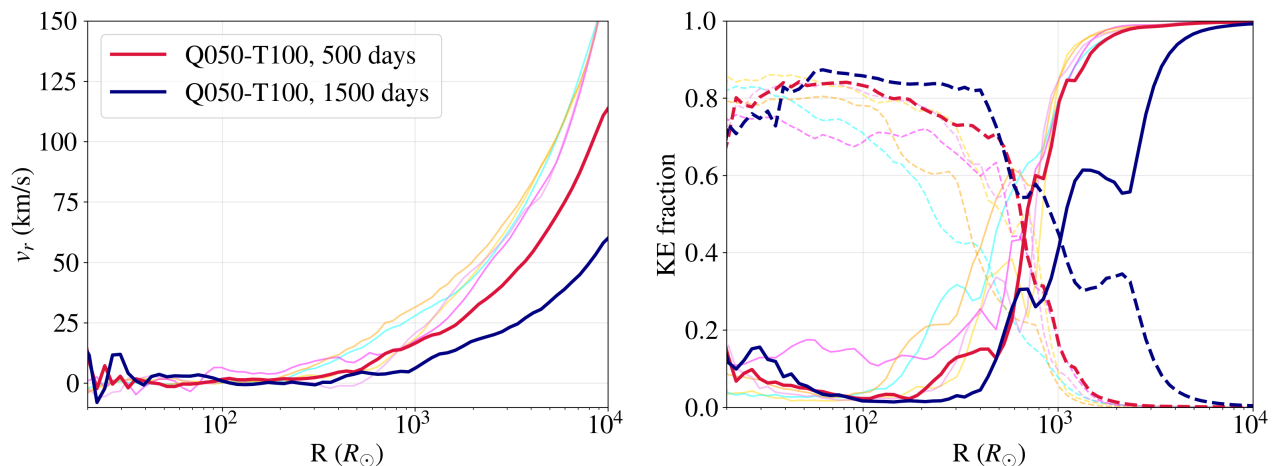


FIG. 10. *Left*: Radial velocity (v_r) as a function of radius for the runs Q025, Q050, Q075, Q100, and Q050-NCR at $t = 500$ days (faint lines), and for Q050-T100 at $t = 500$ and 1500 days (bright red and navy lines, respectively). *Right*: Fraction of kinetic energy in the azimuthal (ϕ , dashed lines) and radial (r , solid lines) components as a function of radius.

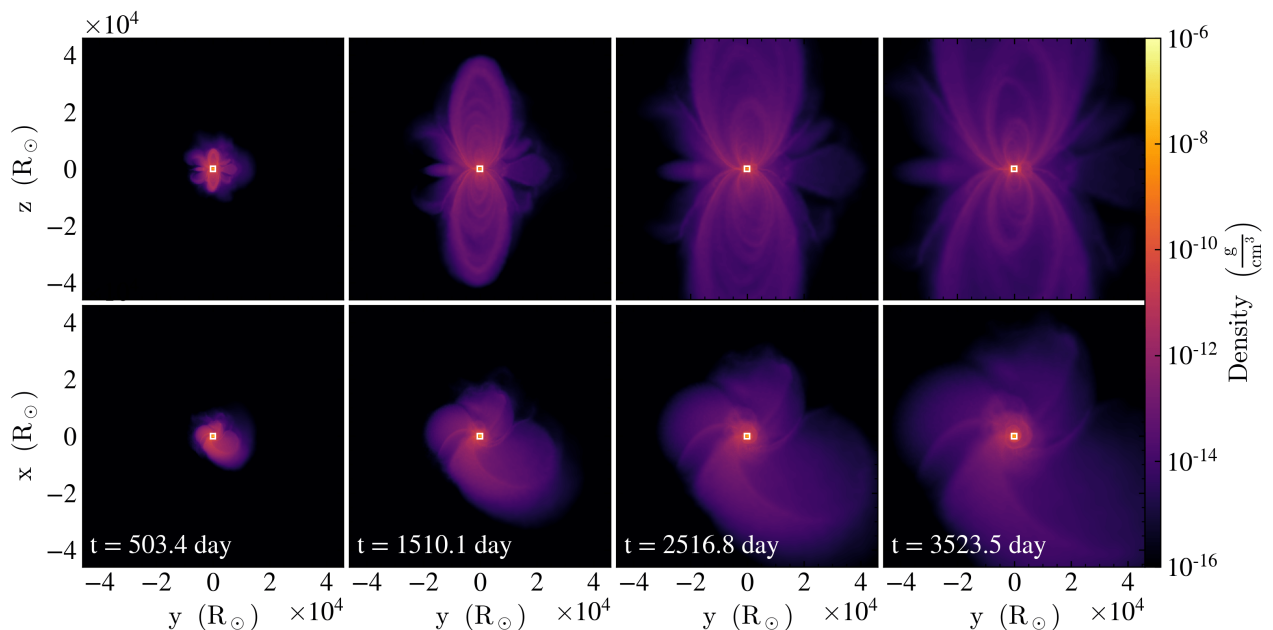


FIG. 11. Density distribution at a larger box for the same run (Q050-T100), projections, and times as in Figs. 7 and 8. The small white square at the center indicates the size of the entire region shown in Fig. 8, where the CBD resides.

include magnetic fields. The formation of a CBD and the resulting collimated outflows therefore do not require MHD effects, consistent with the results of Gagnier and Pejcha [22]. Moreover, we have found collimated outflows for all mass ratios, in the cases with and without corotation and for the different temperature floor, but not for the HLLC riemann solver. Which shows that numerics are the highest source of impact in the formation of such structures.

Very likely the collimation mechanism is similar to that described by Icke [46], where the opening angle is determined primarily by the geometry of outflows emerging

above a thick disk. In that work the resulting bi-conical structure is defined by the region where an outward force (radiation pressure in their case, gas pressure in our simulations) overcomes gravity and allows material to escape. Nevertheless, magnetic fields have been detected in some WFs and are expected to influence the outflow properties. As noted by Vetter *et al.* [44], magnetic fields can affect the final separation, turbulence, and local asymmetries. Our results therefore suggest that while magnetic fields may modify the detailed structure of the outflows, wide-angle collimated outflows can already arise from purely hydrodynamical processes.

B. Speed of the outflow

The maximum speed of the ejecta (v_{\max} at $\theta = 0^\circ$) begins at approximately 250 km s^{-1} and gradually decreases to about 200 km s^{-1} during the evolution. These velocities are comparable to the escape speed of the central binary. At a distance of $100 R_\odot$ from the binary, the escape speed in all simulations is below 100 km s^{-1} , which is smaller than the velocity corresponding to 1σ of the Gaussian distribution ($0.606 v_{\max}$). This indicates that the outflowing material exceeds the local escape speed and is therefore able to escape the system.

A comparable dependence on the system parameters was reported by Ondratschek *et al.* [47], where the maximum velocity varied between $\sim 120 \text{ km s}^{-1}$ and 60 km s^{-1} depending on the mass ratio. In their case, the final separation of their simulations is larger, which explains the smaller escape speeds and thus, velocities. In general, these studies indicate that the characteristic velocity of the outflow is of the same order as the escape speed of the central binary. Observationally, the velocities predicted by our simulations are consistent with those measured in some of the fastest WFs, such as IRAS 16342–3814 ($\sim 180 \text{ km s}^{-1}$; Claussen *et al.* 48) and IRAS 16552–3050 ($\sim 170 \text{ km s}^{-1}$; Suárez *et al.* 49).

C. Formation of bipolar structures

In addition, for the Q050-T100 simulation, we evolved the system up to 3500 days to understand how the envelope morphology develops at later times. A detailed study of the long-term evolution of the disk and its impact on the central binary is left for future work. Nevertheless, the extended evolution allows us to examine the large-scale morphology of the ejecta at later times.

From Fig. 11, we note the bipolar structure that form in the outflow is clearly defined. The overall morphology is consistent with the bipolar structures commonly observed in PNe. This behavior is also reflected in Fig. 13, which shows that the total amount of mass in the polar regions increases over time, which is a consequence of the envelope being preferentially ejected from the CBD to the collimated outflows. This progressive redistribution of mass toward the polar directions further reinforces the emergence of a bipolar morphology for CEE events.

VII. INSIGHTS FOR FUTURE WORKS

In this section, we present some speculative ideas that can serve as inspiration for future work. We do not claim them to be true, but as interesting avenues that could be explored.

A. Orbital decay traced by "jet" acceleration?

WF sources show outflows velocities ranging from $\sim 30 \text{ km s}^{-1}$ to several hundred km s^{-1} . One question is whether this diversity reflects differences in system parameters or different evolutionary stages, and the available evidence suggests that both effects may play a role. In particular, WFs show evidence for acceleration of the collimated outflows over time. This is supported by multi-epoch observations of individual objects [50] as well as population studies indicating that low-velocity WFs are systematically younger than high-velocity WFs [51]. Together, these results suggest that the characteristic outflow velocity in WFs increases as the system evolves. One possible explanation is that the low-density winds emerging from the central regions of the post-AGB star become faster as the stellar core heats up [52].

There is, however, another possibility. If the collimated outflow velocity provides an order-of-magnitude estimate of the escape speed from the launching region, the observed evolution could instead reflect a decrease in the orbital separation of the central binary. Adopting a characteristic total mass of $\sim 1 M_\odot$, simple estimates indicate that an increase in velocity from tens to a few hundred km s^{-1} corresponds to a contraction from separations of order tens of R_\odot to a few R_\odot . These values are consistent with the separations obtained in AGB CEE simulations [18] after the plunge-in phase, as well as with those inferred for observations of post-CEE close binaries [53]. This interpretation may naturally explain the observed acceleration of WF collimated outflows.

Additional support for this scenario comes from the high mass-loss rates inferred in some WFs, which can reach $\sim 10^{-3} M_\odot \text{ yr}^{-1}$. Such values are difficult to reconcile with low-density winds originating from the stellar core, suggesting that the outflows may instead be powered by envelope being ejected with the help from the release of orbital energy from the compact binary. In this picture, the increase in outflow velocity would likely follow naturally from the gradual orbital decay.

Finally, although thin CBDs do not always lead to orbital decay and may in some cases cause orbital widening depending on the system parameters, thick CBDs are generally expected to lead to orbital shrinkage, even though this regime remains poorly explored in current simulations [see 36, for a discussion]. Continued orbital decay in the presence of a thick CBD would therefore provide a natural mechanism for producing the increasing the velocities of collimated outflows observed in WFs and explain the discrepancy between the separations of close binary systems and CEE simulations.

A final possibility is that the angular momentum deposited during the plunge allows the still-bound envelope to reorganize into a thick CBD or torus-like structure surrounding the central binary. The main difference between this interpretation and those mediated primarily by drag is that the central binary clears a low-density cavity in its immediate surroundings. As a consequence,

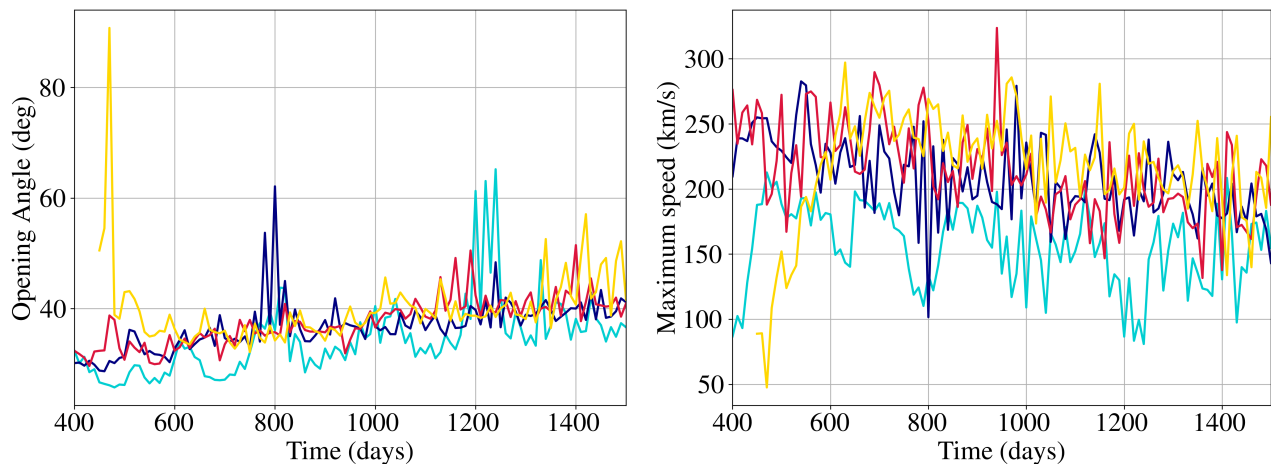


FIG. 12. *Left*: Opening angle and central angle versus time for different mass ratios. *Right*: Maximum speed versus time for different mass ratios. The colors represent the runs Q025 (cyan), Q050 (purple), Q075 (red), and q100 (yellow). The run Q100 takes longer to transition into the spiral-in phase and hence have a lower speed and large radii at the first 50 days, before settling in similar values to the other runs.

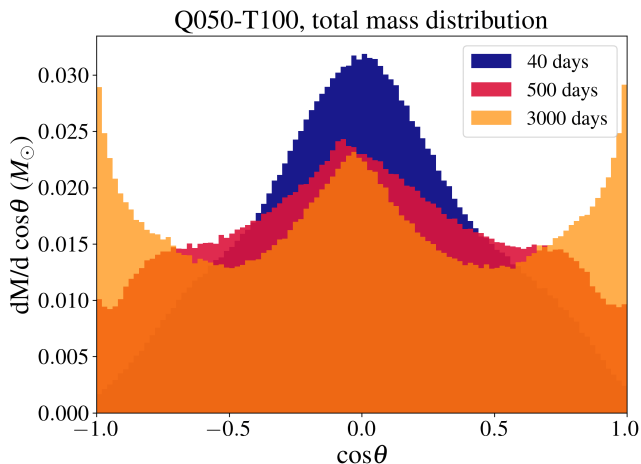


FIG. 13. Mass distribution per $\cos(\theta)$ for the entire domain for the Q050-T100 run, at 40 (blue), 500 (red) and 3000 (orange) days.

the binary no longer interacts mainly through dynamical friction with a quasi-spherical envelope. Instead, the orbital evolution, which for CBDs does not necessarily correspond to orbital decay and can even lead to orbital widening, is governed by the exchange of angular momentum between the binary and the CBD. This interaction may involve several mechanisms, including accretion onto the central stars, Lindblad resonances, and corotation torques [see, e.g. 36]. Episodic events may also occur. For example, if the disk is sufficiently massive, gravitational instabilities analogous to those invoked in FU Orionis systems may develop [see, e.g. 54]. Such instabilities could temporarily enhance the accretion rate, allowing significant amounts of envelope material to flow

into the central cavity and potentially producing short episodes of increased drag.

B. Other CEE-related post-AGB/RGB objects

The Red Rectangle Nebula [55] and other similar objects are post-AGB/pre-PNe systems with close binaries and a CBD. These objects are somewhat intriguing because they have wider separations compared to other post-CEE systems, which has led to the proposition that they may have gone through a somewhat failed CEE event, or grazing envelope evolution. Tuna and Metzger [56] have also proposed that the larger separation is a consequence of the CBD, given that they are known to be able to both widen or shrink the orbit depending on their properties and the mass ratio between the stars.

Here we propose a different scenario that can be explored in future work: the differences between Red Rectangle-like nebulae and WFs can be explained if CEE happened at different AGB stages. For Red Rectangle systems, CEE likely happens with a more evolved AGB opposed to WFs, that happens with AGBs before the third dredge-up. As discussed in Borges [23], larger stellar radii will inevitably lead to larger final separations, and those systems can have separations ranging from a few tens or even hundreds of R_{\odot} , simply because drag stalls earlier in a less dense and more extended envelope. This explains why both WFs and the red rectangle nebulae have found similar morphologies [55].

Interestingly, this is not unique to post-AGBs. A similar morphology with collimated outflows and wide opening angles is also seen in post-RGB objects such as the Boomerang Nebula [57]. This suggests that the most robust observational signature of a CEE event may be the wide collimated outflows, formed due to the redistribu-

tion of angular momentum in the still-bound envelope and formation of a CBD. This shows that, even though our simulations were done with a RGB giant, the results translates well for post-AGB systems such as WFs.

VIII. CONCLUSIONS

CEE has remained an unsolved problem in stellar astrophysics for the last 50 years. We still lack not only a predictive model but also a clear description of how each phase evolves. In this paper, we argue that we may be gradually converging toward a qualitative picture of how CEE evolves, although we remain far from having a predictive analytical or 1D model.

An important open question concerns the last phase of CEE, the spiral-in phase. In this case, we argue that both numerical simulations and observations point toward the same scenario: the still-bound envelope re-distributes into a thick CBD, and the envelope is then preferentially ejected in the polar direction through collimated outflows. In this work, we have described analytically how this disk is structured. We conclude by noting that the results presented here may provide useful initial conditions for future analytical or numerical modeling studies of the spiral-in phase of CEE. Furthermore, we find that changes in mass ratio, corotation, or floor temperature can modify some disk properties but do not prevent the formation of a CBD and collimated outflows.

We have also compared this morphology and kinematics with WF observations. Since we have not followed the evolution of the system for ~ 200 years, it is not yet possible to compare the full evolution of the simulations with WFs, which we leave for future work. We find that the collimated outflow speeds predicted by our model are comparable to the escape speed of the system and are also consistent with some of the fastest WFs. We also

find that the opening angles of the collimated outflows are wide and similar to those observed. This suggests that the collimation in WFs likely arises from geometric constraints: the thick equatorial disk naturally forces the ejected envelope into collimated polar flows.

We conclude the paper by discussing some ideas inspired by WF observations and other post-CEE objects that may motivate future work. These ideas are speculative, and we do not claim that these models are necessarily correct, but rather that they represent possible avenues worth exploring. First, WFs have been observed to exhibit collimate outflow speeds that increase with time, which may reflect a decreasing binary separation. Second, the differences between WFs and other post-AGB systems with thin disks (such as the Red Rectangle) may reflect the evolutionary stage at which CEE occurred, with the Red Rectangle representing a system with a more evolved AGB star and WFs corresponding to less evolved systems.

ACKNOWLEDGMENTS

SVB acknowledges support from the NASA ATP program (NNH23ZDA001N-ATP) and the College of Letters and Science at UWM through the Chancellor's Graduate Student Award and the Research Excellence Award. PC acknowledges support from the NASA ATP program through NASA grant NNH17ZDA001N-ATP and National Science Foundation (NSF) via AST-2108269 and AST-2307885.

DATA AVAILABILITY

After the submission, a link will be provided. For now, data is available only upon request to the corresponding author.

-
- [1] N. Ivanova, S. Justham, and P. Ricker, *Common Envelope Evolution* (2020).
 - [2] F. K. Röpke and O. De Marco, Simulations of common-envelope evolution in binary stellar systems: physical models and numerical techniques, *Living Reviews in Computational Astrophysics* **9**, 2 (2023), arXiv:2212.07308 [astro-ph.SR].
 - [3] R. Tytenda, M. Hajduk, T. Kamiński, A. Udalski, I. Soszyński, M. K. Szymański, M. Kubiak, G. Pietrzyński, R. Poleski, L. Wyrzykowski, and K. Ulaczyk, V1309 Scorpii: merger of a contact binary, *A&A* **528**, A114 (2011), arXiv:1012.0163 [astro-ph.SR].
 - [4] K. B. Kwitter and R. B. C. Henry, Planetary Nebulae: Sources of Enlightenment, *PASP* **134**, 022001 (2022), arXiv:2110.13993 [astro-ph.SR].
 - [5] B. Balick and A. Frank, Shapes and Shaping of Planetary Nebulae, *Annual Review of Astronomy and Astrophysics* **40**, 439 (2002).
 - [6] D. Jones and H. M. J. Boffin, Binary stars as the key to understanding planetary nebulae, *Nature Astronomy* **1**, 0117 (2017), arXiv:1705.00283 [astro-ph.SR].
 - [7] R. Sahai and J. T. Trauger, Multipolar Bubbles and Jets in Low-Excitation Planetary Nebulae: Toward a New Understanding of the Formation and Shaping of Planetary Nebulae, *AJ* **116**, 1357 (1998).
 - [8] Q. A. Parker, A. Acker, D. J. Frew, M. Hartley, A. E. J. Peyaud, F. Ochsenbein, S. Phillipps, D. Russeil, S. F. Beaulieu, M. Cohen, J. Köppen, B. Miszalski, D. H. Morgan, R. A. H. Morris, M. J. Pierce, and A. E. Vaughan, The Macquarie/AAO/Strasbourg H α Planetary Nebula Catalogue: MASH, *MNRAS* **373**, 79 (2006).
 - [9] I. González-Santamaría, M. Manteiga, A. Manchado, A. Ulla, C. Dafonte, and P. López Varela, Planetary nebulae in Gaia EDR3: Central star identification, properties, and binarity, *A&A* **656**, A51 (2021), arXiv:2109.12114 [astro-ph.GA].

- [10] G. García-Segura, P. M. Ricker, and R. E. Taam, Common Envelope Shaping of Planetary Nebulae, *ApJ* **860**, 19 (2018), arXiv:1804.09309 [astro-ph.SR].
- [11] Y. Zou, A. Frank, Z. Chen, T. Reichardt, O. De Marco, E. G. Blackman, J. Nordhaus, B. Balick, J. Carroll-Nellenback, L. Chamandy, and B. Liu, Bipolar planetary nebulae from outflow collimation by common envelope evolution, *MNRAS* **497**, 2855 (2020), arXiv:1912.01647 [astro-ph.SR].
- [12] R. A. Cala, J. F. Gómez, L. F. Miranda, H. Imai, G. Anglada, I. de Gregorio-Monsalvo, K. Ohnaka, O. Suárez, D. Tafoya, and L. Uscanga, Identification and characterization of nascent planetary nebulae with OH and H₂O masers, *A&A* **703**, A268 (2025), arXiv:2509.15727 [astro-ph.SR].
- [13] T. Khouri, W. H. T. Vlemmings, D. Tafoya, A. F. Pérez-Sánchez, C. Sánchez Contreras, J. F. Gómez, H. Imai, and R. Sahai, Observational identification of a sample of likely recent common-envelope events, *Nature Astronomy* **6**, 275 (2021), arXiv:2112.09689 [astro-ph.SR].
- [14] F. Meyer and E. Meyer-Hofmeister, Formation of cataclysmic binaries through common envelope evolution., *A&A* **78**, 167 (1979).
- [15] N. Ivanova and J. L. A. Nandez, Common envelope events with low-mass giants: understanding the transition to the slow spiral-in, *MNRAS* **462**, 362 (2016), arXiv:1606.04923 [astro-ph.SR].
- [16] V. Valsan, S. V. Borges, L. Prust, and P. Chang, Envelope ejection and the transition to homologous expansion in common-envelope events, *MNRAS* **526**, 5365 (2023), arXiv:2309.15921 [astro-ph.SR].
- [17] L. J. Prust and P. Chang, Common envelope evolution on a moving mesh, *MNRAS* **486**, 5809 (2019), arXiv:1904.09256 [astro-ph.SR].
- [18] C. Sand, S. T. Ohlmann, F. R. N. Schneider, R. Pakmor, and F. K. Röpkke, Common-envelope evolution with an asymptotic giant branch star, *A&A* **644**, A60 (2020), arXiv:2007.11000 [astro-ph.SR].
- [19] L. Chamandy, A. Frank, E. G. Blackman, J. Carroll-Nellenback, B. Liu, Y. Tu, J. Nordhaus, Z. Chen, and B. Peng, Accretion in common envelope evolution, *MNRAS* **480**, 1898 (2018), arXiv:1805.03607 [astro-ph.SR].
- [20] T. A. Reichardt, O. De Marco, R. Iaconi, C. A. Tout, and D. J. Price, Extending common envelope simulations from Roche lobe overflow to the nebular phase, *MNRAS* **484**, 631 (2019), arXiv:1809.02297 [astro-ph.SR].
- [21] M. Vetter, F. K. Röpkke, F. R. N. Schneider, R. Pakmor, S. T. Ohlmann, M. Y. M. Lau, and R. Andrassy, From spherical stars to disk-like structures: 3D common-envelope evolution of massive binaries beyond inspiral, *A&A* **691**, A244 (2024), arXiv:2410.07841 [astro-ph.SR].
- [22] D. Gagnier and O. Pejcha, Journey to the center of the common envelope evolution: Inner dynamics of the post-dynamical inspiral, *A&A* **697**, A68 (2025), arXiv:2412.04419 [astro-ph.SR].
- [23] S. V. Borges, A Correlation between the Final Separation and Mass Ratio from Common-envelope Simulations, *ApJ* **998**, 34 (2026), arXiv:2511.02150 [astro-ph.SR].
- [24] P. Chang, J. Wadsley, and T. R. Quinn, A moving-mesh hydrodynamic solver for ChaNGa, *MNRAS* **471**, 3577 (2017), arXiv:1707.05333 [astro-ph.IM].
- [25] P. Jetley, F. Gioachin, C. Mendes, L. V. Kale, and T. Quinn, Massively parallel cosmological simulations with changa, in *2008 IEEE International Symposium on Parallel and Distributed Processing* (2008) pp. 1–12.
- [26] P. Jetley, L. Wesolowski, F. Gioachin, L. Kalé, and T. Quinn, Scaling hierarchical n-body simulations on gpu clusters (2010) pp. 1 – 11.
- [27] H. Menon, L. Wesolowski, G. Zheng, P. Jetley, L. Kale, T. Quinn, and F. Governato, Adaptive techniques for clustered N-body cosmological simulations, *Computational Astrophysics and Cosmology* **2**, 1 (2015), arXiv:1409.1929 [astro-ph.IM].
- [28] A. Spaulding and P. Chang, The effect of impact parameter on tidal disruption events, *MNRAS* **501**, 1748 (2021), arXiv:2010.07318 [astro-ph.HE].
- [29] L. E. Williams, P. Chang, E. M. Levesque, and T. R. Quinn, Neutron Star-Main Sequence Collisions Robustly Form Dynamically Stable Thorne-Zytkow Objects, *ApJ* **993**, 61 (2025), arXiv:2510.16129 [astro-ph.SR].
- [30] B. Paxton, L. Bildsten, A. Dotter, F. Herwig, P. Lesaffre, and F. Timmes, Modules for Experiments in Stellar Astrophysics (MESA), *ApJS* **192**, 3 (2011), arXiv:1009.1622 [astro-ph.SR].
- [31] B. Paxton, M. Cantiello, P. Arras, L. Bildsten, E. F. Brown, A. Dotter, C. Mankovich, M. H. Montgomery, D. Stello, F. X. Timmes, and R. Townsend, Modules for Experiments in Stellar Astrophysics (MESA): Planets, Oscillations, Rotation, and Massive Stars, *ApJS* **208**, 4 (2013), arXiv:1301.0319 [astro-ph.SR].
- [32] B. Paxton, P. Marchant, J. Schwab, E. B. Bauer, L. Bildsten, M. Cantiello, L. Dessart, R. Farmer, H. Hu, N. Langer, R. H. D. Townsend, D. M. Townsley, and F. X. Timmes, Modules for Experiments in Stellar Astrophysics (MESA): Binaries, Pulsations, and Explosions, *ApJS* **220**, 15 (2015), arXiv:1506.03146 [astro-ph.SR].
- [33] B. Paxton, J. Schwab, E. B. Bauer, L. Bildsten, S. Blinnikov, P. Duffell, R. Farmer, J. A. Goldberg, P. Marchant, E. Sorokina, A. Thoul, R. H. D. Townsend, and F. X. Timmes, Modules for Experiments in Stellar Astrophysics (MESA): Convective Boundaries, Element Diffusion, and Massive Star Explosions, *ApJS* **234**, 34 (2018), arXiv:1710.08424 [astro-ph.SR].
- [34] B. Paxton, R. Smolec, J. Schwab, A. Gaudsichy, L. Bildsten, M. Cantiello, A. Dotter, R. Farmer, J. A. Goldberg, A. S. Jermyn, S. M. Kanbur, P. Marchant, A. Thoul, R. H. D. Townsend, W. M. Wolf, M. Zhang, and F. X. Timmes, Modules for Experiments in Stellar Astrophysics (MESA): Pulsating Variable Stars, Rotation, Convective Boundaries, and Energy Conservation, *ApJS* **243**, 10 (2019), arXiv:1903.01426 [astro-ph.SR].
- [35] A. S. Jermyn, E. B. Bauer, J. Schwab, R. Farmer, W. H. Ball, E. P. Bellinger, A. Dotter, M. Joyce, P. Marchant, J. S. G. Mombarg, W. M. Wolf, T. L. Sunny Wong, G. C. Cinquegrana, E. Farrell, R. Smolec, A. Thoul, M. Cantiello, F. Herwig, O. Toloza, L. Bildsten, R. H. D. Townsend, and F. X. Timmes, Modules for Experiments in Stellar Astrophysics (MESA): Time-dependent Convection, Energy Conservation, Automatic Differentiation, and Infrastructure, *ApJS* **265**, 15 (2023), arXiv:2208.03651 [astro-ph.SR].
- [36] D. Lai and D. J. Muñoz, Circumbinary Accretion: From Binary Stars to Massive Binary Black Holes, *Annual Review of Astronomy and Astrophysics* **61**, 517 (2023), arXiv:2211.00028 [astro-ph.HE].
- [37] P. C. Duffell, A. J. Dittmann, D. J. D’Orazio, A. Franchini, K. M. Kratter, A. B. T. Penzlin, E. Ragusa, M. Si-

- wek, C. Tiede, H. Wang, J. Zrake, A. M. Dempsey, Z. Haiman, A. Lupi, M. Pirog, and G. Ryan, The Santa Barbara Binary-disk Code Comparison, *ApJ* **970**, 156 (2024), arXiv:2402.13039 [astro-ph.SR].
- [38] C. Tiede, J. Zrake, A. MacFadyen, and Z. Haiman, Gas-driven Inspiral of Binaries in Thin Accretion Disks, *ApJ* **900**, 43 (2020), arXiv:2005.09555 [astro-ph.GA].
- [39] A. Kashi and N. Soker, A circumbinary disc in the final stages of common envelope and the core-degenerate scenario for Type Ia supernovae, *MNRAS* **417**, 1466 (2011), arXiv:1105.5698 [astro-ph.SR].
- [40] D. Wei, F. R. N. Schneider, P. Podsiadlowski, E. Laplace, F. K. Röpkke, and M. Vetter, Evolution and final fate of massive post-common-envelope binaries, *A&A* **688**, A87 (2024), arXiv:2311.07278 [astro-ph.HE].
- [41] R. Valli, C. Tiede, A. Vigna-Gómez, J. Cuadra, M. Siwek, J.-Z. Ma, D. J. D’Orazio, J. Zrake, and S. E. de Mink, Long-term evolution of binary orbits induced by circumbinary disks, *A&A* **688**, A128 (2024), arXiv:2401.17355 [astro-ph.HE].
- [42] J. F. Gómez, G. Niccolini, O. Suárez, L. F. Miranda, J. R. Rizzo, L. Uscanga, J. A. Green, and I. de Gregorio-Monsalvo, ALMA imaging of the nascent planetary nebula IRAS 15103-5754, *MNRAS* **480**, 4991 (2018), arXiv:1808.03681 [astro-ph.SR].
- [43] K. Murakawa and H. Izumiura, Dust shell model of the water fountain source IRAS 16342-3814, *A&A* **544**, A58 (2012), arXiv:1207.4944 [astro-ph.SR].
- [44] M. Vetter, F. K. Röpkke, F. R. N. Schneider, R. Pakmor, S. Ohlmann, J. Morán-Fraile, M. Y. M. Lau, G. Leidi, D. Gagnier, and R. Andrassy, Magnetically driven outflows in the 3D common envelope evolution of massive stars, *A&A* **698**, A133 (2025), arXiv:2504.12213 [astro-ph.SR].
- [45] L. Uscanga, H. Imai, J. F. Gómez, D. Tafuya, G. Orosz, T. P. McCarthy, Y. Hamae, and K. Amada, Evolution of the Outflow in the Water Fountain Source IRAS 18043-2116, *ApJ* **948**, 17 (2023), arXiv:2303.01583 [astro-ph.SR].
- [46] V. Icke, Are bipolar nebulae biconical ?, *ApJ* **247**, 152 (1981).
- [47] P. A. Ondratschek, F. K. Röpkke, F. R. N. Schneider, C. Fendt, C. Sand, S. T. Ohlmann, R. Pakmor, and V. Springel, Bipolar planetary nebulae from common-envelope evolution of binary stars, *A&A* **660**, L8 (2022), arXiv:2110.13177 [astro-ph.SR].
- [48] M. J. Claussen, R. Sahai, and M. R. Morris, The Motion of Water Masers in the Pre-Planetary Nebula IRAS 16342-3814, *ApJ* **691**, 219 (2009), arXiv:0810.1271 [astro-ph].
- [49] O. Suárez, J. F. Gómez, and L. F. Miranda, VLA Observations of the “Water Fountain” IRAS 16552-3050, *ApJ* **689**, 430 (2008), arXiv:0809.0392 [astro-ph].
- [50] G. Orosz, J. F. Gómez, H. Imai, D. Tafuya, J. M. Torrelles, R. A. Burns, P. Frau, M. A. Guerrero, L. F. Miranda, M. A. Perez-Torres, G. Ramos-Larios, J. R. Rizzo, O. Suárez, and L. Uscanga, Rapidly evolving episodic outflow in IRAS 18113-2503: clues to the ejection mechanism of the fastest water fountain, *MNRAS* **482**, L40 (2019), arXiv:1809.07505 [astro-ph.SR].
- [51] R. A. Cala, L. F. Miranda, J. F. Gómez, and K. Ohnaka, Low- and high-velocity “water fountains”: Different evolutionary stages, *A&A* **703**, L7 (2025), arXiv:2510.01856 [astro-ph.SR].
- [52] H. J. G. L. M. Lamers and E. M. Levesque, *Understanding Stellar Evolution* (2017).
- [53] M. U. Kruckow, P. G. Neunteufel, R. Di Stefano, Y. Gao, and C. Kobayashi, A Catalog of Potential Post-Common Envelope Binaries, *ApJ* **920**, 86 (2021), arXiv:2107.05221 [astro-ph.SR].
- [54] K. Kratter and G. Lodato, Gravitational Instabilities in Circumstellar Disks, *Annual Review of Astronomy and Astrophysics* **54**, 271 (2016), arXiv:1603.01280 [astro-ph.SR].
- [55] A. B. Men’shchikov, D. Schertl, P. G. Tuthill, G. Weigelt, and L. R. Yungelson, Properties of the close binary and circumbinary torus of the ι ASTROBJ $_i$ Red Rectangle/ASTROBJ $_i$, *A&A* **393**, 867 (2002), arXiv:astro-ph/0206189 [astro-ph].
- [56] S. Tuna and B. D. Metzger, Long-term Evolution of Massive-star Post-common-envelope Circumbinary Disks and the Environments of Fast Luminous Transients, *ApJ* **955**, 125 (2023), arXiv:2306.10111 [astro-ph.HE].
- [57] R. Sahai, W. H. T. Vlemmings, P. J. Huggins, L.-Å. Nyman, and I. Gonidakis, ALMA Observations of the Coldest Place in the Universe: The Boomerang Nebula, *ApJ* **777**, 92 (2013), arXiv:1308.4360 [astro-ph.SR].